SEPARATED AND HIGH-LIFT FLOWS OVER SINGLE AND MULTI-ELEMENT AIRFOILS

Torbjörn Larsson
Saab Military Aircraft
Linköping, Sweden

Abstract

The current work presents Navier-Stokes results for single and multi-element airfoils at conditions close to stall. Influences from turbulence are accounted for by two different turbulence models, a two-equation κ-ε model and a full Reynolds stress model. In general very good agreement with experiments is found.

Special emphasis is put on the drag prediction ability for high-lift multi-element flows since this topic has proven to be quite problematic. Different drag integration methods are applied for comparison. The farfield boundary conditions are shown to be of great importance for an accurate prediction. By use of a vortex correction at the farfield boundary a significant improvement is demonstrated in the drag predictions.

As a good example of how the use of advanced CFD methods nowadays can support and bring new knowledge and valuable insight into an ongoing aircraft project results are shown from an extensive numerical evaluation of the wing and horizontal stabilizer of the new SAAB 2000 regional aircraft.

A reshaping of the stabilizer profile is made, based on computed displacement thickness and results obtained from an inverse design calculation. A clear drag reduction at cruise conditions is obtained in the calculations which later on also was verified in flight test.

Nomenclature

α	Angle of attack
c	Airfoil chord
C_d	Drag coefficient = $\frac{Drag}{q_\infty c}$
C_f	Skin friction coefficient = $\frac{\tau_w}{q_\infty}$
C_l	Lift coefficient = $\frac{Lift}{q_\infty c}$
C_p	Pressure coefficient = $\frac{p - p_\infty}{q_\infty}$
δ	Wing element deflection angle
δ^*	Boundary layer displacement thickness
Γ	Circulation = $\frac{1}{2} q_\infty C_l c$
M_∞	Freestream Mach number
p	Static pressure
q_∞	Freestream dynamic pressure
Re	Reynolds number
τ_w	Wall shear stress
U_i	Mean velocity component
u_i	Fluctuating velocity component
x_i	Cartesian coordinate component

Introduction

An accurate prediction of separated flow over a wing is still an unsolved problem. Even a two-dimensional computation over a multi-element airfoil close to stall is a formidable problem due to the complex geometry producing complicated viscous flows. Within the aircraft industry design of e.g. high-lift devices is an important topic which can have a major influence on the overall economy and safety of the aircraft. Increases in maximum lift coefficient and improved lift over drag characteristics will lead to reductions in both landing and take-off speeds. Hence, development and improvements of numerical tools capable of handling separated viscous flows are of great interest.

The design of high-lift devices has, in a historical perspective, totally relied on experimental investigations. Nowadays, however, CFD tools have come to play an increasing role. Especially the possibility to simulate the full-scale Reynolds number makes these CFD methods particularly useful.

Today, computational methods for high-lift systems based on the viscid-inviscid interaction approach with integral methods for boundary layers and wakes are quite common. Although fast solutions can be obtained with these methods it is highly desirable to have a numerical method that captures the flow physics in a more detailed and adequate way.

With the ever increasing computer capacity and the improved numerical algorithms more interest has been shifted towards the possibility to obtain an accurate prediction of the high-lift characteristics with Navier-Stokes methods.

Some of the flow physics characterizing multi-element airfoils and not found on cruise airfoils are e.g. strong interaction between wakes from up-stream elements and boundary layers on down-stream elements, separated cove flows and significant streamline curvature effects.

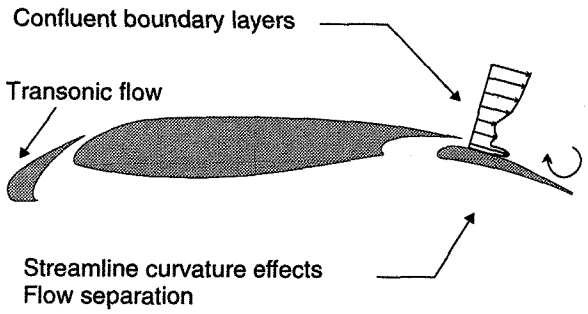

Fig. 1 Multi-element flow characteristics

Thick viscous layers over trailing edge flaps could give flow separation even for conditions well below maximum lift. Transonic flow may also appear over leading edge slats even though the freestream Mach number is as low as 0.2.

For these reasons the demands are high on the numerical methods used in this type of calculations, and one can easily focus on several crucial points that must be treated in an adequate way. One of these is the turbulence modelling and another the grid generation. In some sense contrary to the use of elaborate turbulence models and excessively fine grids stands the demand of moderate computational time which must be fulfilled if the method should be used as an engineering tool in the design process.

The present paper presents results from Navier-Stokes computations for both single-element and multi-element airfoils at conditions near maximum lift. The computational results are compared with wind-tunnel measurements and the agreement is in general very good.

Different turbulence models are applied and some of their major short-comings are pointed out. Utilization of multigrid gives for some of the cases a high convergence speedup resulting in reasonable computational times even on a workstation.

The ability of getting an accurate drag prediction for high-lift cases is investigated and here the treatment of the farfield boundary is shown to be of great importance. Different methods for drag evaluation are also applied for comparison.

Finally, as an example of the increased industrial use of advanced CFD methods results are shown from an extensive aerodynamic evaluation of both tailplane and wing of the SAAB 2000 regional aircraft. Effects of e.g. elevator/flap deflections, varying gap size between airfoil and elevator/flap as well as different geometries are studied applying a Navier-Stokes solver including a κ-ε turbulence model. The outcome of this investigation is used as a design guide and complement to the wind-tunnel measurements and flight tests.

Governing Equations

Integrating the two-dimensional time-dependent compressible Reynolds averaged Navier-Stokes equations written in conservative form over an arbitrary quadrilateral cell $\Omega_{i,j}$ yields

$$\int\int_{\Omega_{i,j}} \frac{\partial W}{\partial t} dS + \oint_{\partial\Omega_{i,j}} \mathcal{H}(W)\,\hat{n}\,ds = 0 \tag{1}$$

Here the vector of conserved variables $W=(\rho, \rho U, \rho V, \rho E)^T$ contains density ρ, the Cartesian mean velocity components U, V and total energy per unit mass E. The total energy E is given by

$$E = \frac{p}{\rho(\gamma-1)} + \frac{1}{2}(U^2+V^2) \tag{2}$$

where γ is the ratio of specific heats and p is the static pressure.

The flux tensor $\mathcal{H}$ is composed of convective, viscous and turbulent parts

$$\mathcal{H} = (F^c - F^v - F^t)\,e_x + (G^c - G^v - G^t)\,e_y \tag{3}$$

in the x and y coordinate directions, respectively.

The convective fluxes are given by

$$F^c = \begin{bmatrix} \rho U \\ \rho U^2 + p \\ \rho UV \\ \rho UH \end{bmatrix}, \quad G^c = \begin{bmatrix} \rho V \\ \rho UV \\ \rho V^2 + p \\ \rho VH \end{bmatrix} \tag{4}$$

while the viscous and turbulent fluxes are given by

$$F^v + F^t = \begin{bmatrix} 0 \\ \tau_{xx} - \overline{\rho u^2} \\ \tau_{xy} - \overline{\rho uv} \\ U(\tau_{xx} - \overline{\rho u^2}) + V(\tau_{xy} - \overline{\rho uv}) - q_x \end{bmatrix} \tag{5a}$$

$$G^v + G^t = \begin{bmatrix} 0 \\ \tau_{yx} - \overline{\rho uv} \\ \tau_{yy} - \overline{\rho v^2} \\ U(\tau_{xy} - \overline{\rho uv}) + V(\tau_{yy} - \overline{\rho v^2}) - q_y \end{bmatrix} \tag{5b}$$

$H = E + p/\rho$ is the stagnation enthalpy, q_x, q_y the heat fluxes and u, v the fluctuating velocity components with an overbar indicating mean values.

For a Newtonian fluid the stress tensor τ_{ij} can be expressed in terms of the mean velocity gradients and the viscosity coefficient μ as

$$\tau_{ij} = \mu\left(\frac{\partial U_i}{\partial x_j} + \frac{\partial U_j}{\partial x_i} - \frac{2}{3}\delta_{ij}\frac{\partial U_m}{\partial x_m}\right) \tag{6}$$

with δ_{ij} being the Kronecker delta.

Turbulence Modelling

Due to the non-linear character of the convective terms in the Navier-Stokes equations the Reynolds averaging process has introduced unknown second order correlations. A turbulence model approximates correlations of a certain order in terms of lower order known correlations and/or mean flow quantities in order to arrive at a closed set of equations.

The Two-layer κ-ε Model (KE)

Applying the Boussinesq eddy viscosity concept the Reynolds stresses $-\rho\overline{u_i u_j}$ and the heat fluxes q_i appearing in equation (5) can be expressed as

$$-\rho\overline{u_i u_j} = \mu_t\left(\frac{\partial U_i}{\partial x_j}+\frac{\partial U_j}{\partial x_i}-\frac{2}{3}\delta_{ij}\frac{\partial U_m}{\partial x_m}\right)-\frac{2}{3}\delta_{ij}\rho\kappa \qquad (7)$$

$$q_i = -\left(\frac{\mu}{Pr}+\frac{\mu_t}{Pr_t}\right)\frac{\partial T}{\partial x_i} \qquad (8)$$

where μ_t is the turbulent viscosity, κ the turbulent kinetic energy and T denotes the temperature. The Prandtl numbers are chosen as $Pr = 0.72$ for laminar and $Pr_t = 0.90$ for turbulent flows.

The turbulent kinetic energy κ and its dissipation rate ε are determined from their own transport equations as stated below

$$\frac{\partial}{\partial x_j}(\rho U_j\kappa) = \frac{\partial}{\partial x_j}\left(\frac{\mu_t}{\sigma_\kappa}\frac{\partial\kappa}{\partial x_j}\right)+P_\kappa-\rho\varepsilon \qquad (9)$$

$$\frac{\partial}{\partial x_j}(\rho U_j\varepsilon) = \frac{\partial}{\partial x_j}\left(\frac{\mu_t}{\sigma_\varepsilon}\frac{\partial\varepsilon}{\partial x_j}\right)+c_{\varepsilon1}\frac{\varepsilon}{\kappa}P_\kappa-c_{\varepsilon2}\frac{\rho\varepsilon^2}{\kappa} \qquad (10)$$

with the production term P_κ defined as

$$P_\kappa = -\rho\overline{u_i u_j}\frac{\partial U_i}{\partial x_j} \qquad (11)$$

The turbulent viscosity μ_t is obtained from κ and ε as

$$\mu_t = c_\mu\rho\frac{\kappa^2}{\varepsilon} \qquad (12)$$

with the constants

$$\sigma_\kappa = 1.0,\ \sigma_\varepsilon = 1.3,\ c_\mu = 0.09,\ c_{\varepsilon1} = 1.44,\ c_{\varepsilon2} = 1.92.$$

This is the standard High-Re Jones/Launder model[1-2].

Near Wall Modelling. The κ-ε equations (9, 10) do not account for the interaction between turbulence and fluid viscosity and do not, therefore, apply to the semi-viscous near wall region.

Hence, in the present work a two-layer model is used with the standard κ-ε model (9, 10) applied in the bulk of the flow while the Wolfshtein one-equation model[3] is adopted near the walls. In this model the standard κ-equation is solved, whereas the energy dissipation ε is specified by

$$\varepsilon = \frac{\kappa^{3/2}}{l_\varepsilon} \qquad (13)$$

The turbulent viscosity is given by

$$\mu_t = c_\mu\rho\sqrt{\kappa}l_\mu \qquad (14)$$

and the turbulent length scales are prescribed as

$$l_\mu = c_l n\,[1-exp\,(-R_n/A_\mu)\,] \qquad (15)$$

$$l_\varepsilon = c_l n\,[1-exp\,(-R_n/A_\varepsilon)\,] \qquad (16)$$

The Reynolds number R_n and the constants are defined as

$$R_n = \rho\frac{\sqrt{\kappa}}{\mu}n \qquad c_l = kc_\mu^{-3/4}$$
$$A_\mu = 70 \qquad A_\varepsilon = 2c_l \qquad (17)$$

where k is the von Karman constant (= 0.41) and n denotes the normal distance from the wall.

The matching line between the two models is chosen along a pre-selected gridline where the minimum value of the turbulent Reynolds number R_n is greater than 200. This ensures that the wall damping effects will become negligible at the matching line and results in typically 15-30 gridlines within the inner layer depending on the actual grid used.

The Reynolds-Stress Model (RSM)

The Reynolds stress model is not, in contrast to the κ-ε model, based on the Boussinesq eddy viscosity hypothesis. Instead, the individual Reynolds stresses are determined directly from their own transport equations.

One key advantage of Reynolds stress models is their ability to account for anisotropy of the turbulence as a consequence of e.g. streamline curvature.

The RSM[4] used in the current work has the form

$$C_{ij} = P_{ij}+D_{ij}-\rho\varepsilon_{ij}+\Phi_{ij} \qquad (18)$$

where the convective term C_{ij} and the production term P_{ij} are exact and do not need any modelling, which is an important property of the RSM. These terms are expressed as

$$P_{ij} = -\rho\overline{u_i u_k}\frac{\partial U_j}{\partial x_k}-\rho\overline{u_j u_k}\frac{\partial U_i}{\partial x_k} \qquad (19)$$

$$C_{ij} = \frac{\partial}{\partial x_k}(\rho U_k\overline{u_i u_j}) \qquad (20)$$

The dissipation term ε_{ij} is modelled using the locally isentropic assumption

$$\varepsilon_{ij} = \frac{2}{3}\delta_{ij}\varepsilon \tag{21}$$

where ε denotes the total scalar dissipation rate.

The modelling of the pressure-strain tensor Φ_{ij}, which controls the redistribution of turbulent energy among the different stresses, constitutes a principal difficulty in closing the Reynolds stress equations.

A widely used closure is the following

$$\Phi_{ij} = \Phi_{ij1} + \Phi_{ij2} + \Phi_{ijw1} + \Phi_{ijw2} \tag{22}$$

with

$$\Phi_{ij1} = -C_1\rho\frac{\varepsilon}{\kappa}\left(\overline{u_i u_j} - \frac{\delta_{ij}}{3}\overline{u_k u_k}\right) \tag{23}$$

$$\Phi_{ij2} = -C_2\rho\left(P_{ij} - \frac{\delta_{ij}}{3}P_{kk}\right) \tag{24}$$

Here, Φ_{ij1} is the linear return-to-isotropy model proposed by Rotta[5], which represents the non-linear interaction of the turbulence with itself and is proportional to the degree of anisotropy of the Reynolds stresses. The so-called rapid term Φ_{ij2} is proportional to the degree of anisotropy of the turbulent energy production.

The Reynolds stress model is formally derived for fully turbulent conditions, i.e. high Reynolds number. Therefore, wall correction terms are included in the pressure-strain tensor to account for the 'echo' effect in the proximity of a solid wall. These are given as

$$\Phi_{ijw1} = C'_1\rho\frac{\varepsilon}{\kappa}\left(\overline{u_k u_m}n_k n_m\delta_{ij} - \frac{3}{2}\overline{u_k u_i}n_k n_j - \frac{3}{2}\overline{u_k u_j}n_k n_i\right)f_l \tag{25}$$

$$\Phi_{ijw2} = C'_2\rho\left(\Phi_{km2}n_k n_m\delta_{ij} - \frac{3}{2}\Phi_{ik2}n_k n_j - \frac{3}{2}\Phi_{jk2}n_k n_i\right)f_l \tag{26}$$

where n equals the wall normal unit vector. The f_l-function reduces the wall correction with increasing wall distance and has the form

$$f_l = \frac{\kappa^{3/2}}{2.55\varepsilon\Delta n} \tag{27}$$

with Δn being the wall normal distance.

A common approach for modelling of the diffusion term D_{ij} is to apply the Generalized Gradient Diffusion Hypothesis (GGDH)[6]

$$D_{ij} = \frac{\partial}{\partial x_k}\left(C_\kappa\rho\overline{u_k u_l}\frac{\kappa}{\varepsilon}\frac{\partial}{\partial x_l}(\overline{u_i u_j})\right) \tag{28}$$

However, a simpler eddy viscosity assumption

$$D_{ij} = \frac{\partial}{\partial x_k}\left(\mu_t\frac{\partial}{\partial x_k}(\overline{u_i u_j})\right) \tag{29}$$

is used in the code at the moment.

The turbulent kinetic energy κ and its dissipation rate ε are determined from the same transport equations used in the κ-ε model, except that the production term P_κ now retains its original form as given in eq. (11).

The turbulent heat fluxes are calculated using the eddy viscosity assumption as given in eq. (8).

The constants have been assigned values according to Gibson and Younis[7]

$$(C_1, C_2, C'_1, C'_2) = (3, 0.3, 0.75, 0.15) \tag{30}$$

Near Wall Modelling. In the near wall region the one-equation model by Wolfshtein[3] is applied in the same way as when using the two-layer κ-ε model. In this inner region the stresses are computed as

$$\rho\overline{uv} = -\mu_t\left(\frac{\partial U}{\partial y} + \frac{\partial V}{\partial x}\right) \tag{31a}$$

$$\rho\overline{u^2} = \rho\kappa\left(\frac{\overline{u^2}}{\kappa}\right)_{outer} \tag{31b}$$

$$\rho\overline{v^2} = \rho\kappa\left(\frac{\overline{v^2}}{\kappa}\right)_{outer} \tag{31c}$$

where μ_t is given in eq. (14) and the ratios $(\overline{u^2}/\kappa)_{outer}$ and $(\overline{v^2}/\kappa)_{outer}$ are taken just outside the matching line. These ratios are supposed to remain constant all the way to the wall.

Numerical Method

The SAAB NS2D code[8] solves the two-dimensional time-dependent compressible Reynolds averaged Navier-Stokes equations (1) written in conservative form. The equations are solved in a structured multiblock domain.

Spatial discretization

The mean flow equations are discretized in space using a cell-centered finite volume approximation. Central differences are used for the convective fluxes. For the viscous fluxes, the gradients of velocity and temperature are evaluated using the gradient theorem on auxiliary cells. The viscous fluxes are then computed in the same way as the convective fluxes. The molecular viscosity is determined from Sutherland's law.

The finite volume discretization leads to a system of ordinary differential equation

$$|\Omega_{i,j}|\frac{dW_{i,j}}{dt} = Q^v{}_{i,j} - Q^c{}_{i,j} \tag{32}$$

where $\Omega_{i,j}$ is the cell area and $Q^v{}_{i,j}$ and $Q^c{}_{i,j}$ are the net viscous and convective fluxes, respectively.

A blending of adaptive second and fourth order artificial dissipation terms are added to the numerical scheme to prevent oscillations in the vicinity of shock-waves and suppress odd/even decoupling in the solution. The second order terms

are directly related to the local second differences of pressure which implies that these terms are small except in regions of large pressure gradients such as in the neighbourhood of shock-waves. Fourth order dissipation is added everywhere except where the second order dissipation is large. In boundary layers the influence of artificial dissipation can be decreased through a local Mach number scaling.

Adding of the artificial dissipation terms results in the following numerical scheme

$$|\Omega_{i,j}|\frac{dW_{i,j}}{dt} = Q^{v}{}_{i,j} - Q^{c}{}_{i,j} + D_{i,j} \qquad (33)$$

with $D_{i,j}$ being the artificial dissipation term.

The stationary κ-ε and Reynolds stress equations are treated implicitly for stability reasons. The transport equations for the turbulent quantities can all be written as

$$\frac{\partial}{\partial x_m}(\rho U_m \Psi) = \frac{\partial}{\partial x_m}(\lambda_\Psi \frac{\partial \Psi}{\partial x_m}) + S^\Psi \qquad (34)$$

where S^Ψ denotes a source term and $\Psi = (\kappa, \varepsilon, \overline{u^2}, \overline{v^2}, \overline{uv})$.

The diffusive terms are discretized using central differences, while for the convective terms a hybrid upwind/central differencing is used[2]. The discretization results in a tridiagonal system of linear algebraic equations which are solved using an ADI method[9]. At each time step the steady equations are updated using an under-relaxation factor of 0.5.

Time Integration

To reach a steady state solution the mean flow equations are integrated in time using an explicit five-step Runge-Kutta scheme where the contribution from the dissipation (artificial and physical) stays frozen after the second stage. Local time steps as well as multigrid technique[10] are available for convergence acceleration. The multigrid technique is based on a Full Approximation Scheme (FAS).

Boundary Conditions

At the airfoil surface no-slip and adiabatic wall conditions are assumed while the far-field boundary conditions are based on the one-dimensional Riemann invariants combined with a velocity correction.

The correction velocities are based on the circulation Γ which is obtained from the computed lift coefficient C_l.[11] This velocity correction allows the farfield boundary to be placed closer to the airfoil without any penalty on the accuracy in the solution. By choosing the circulation Γ = 0 the usual Riemann invariants based on freestream values are recovered.

The turbulent quantities are given some low values in the freestream and transition from laminar to turbulent flow is imposed at prescribed locations by setting the turbulent viscosity, in the cell layer adjacent to the wall, to 1% of the molecular viscosity in the production term (11) appearing in the κ-equation (9).

Grid Generation

Calculations concerning high-Reynolds number turbulent flows make the grid generation an important topic and the location of the grid points may have significant influence on the accuracy of the numerical results. In order to resolve the important physics in boundary layers and wakes, clustering of the cells is necessary in these regions. This clustering should be applied in a way that gives very small stretching close to the airfoil surface.

An accurate resolution of a turbulent boundary layer demands cell-dimensions close to the airfoil surfaces smaller than the extension of the viscous sublayer.

Experimental results suggest that the viscous sublayer spans over approximately $0 < y^+ < 5$. Here y^+ is the dimensionless wall normal distance according to

$$y^+ = \rho \frac{u_\tau}{\mu} n \qquad (35)$$

where μ denotes viscosity, ρ density, n the wall normal distance and u_τ is the so-called friction velocity defined as

$$u_\tau = \sqrt{\frac{\tau_w}{\rho}} \qquad (36)$$

with τ_w equal to the wall shear stress.

Empirical formulas[12] derived for a turbulent boundary layer over a flat plate in an incompressible flow with zero pressure gradient relates the physical wall normal distance n to y^+ as

$$n/x = 5.81 y^+ (Re_x)^{-0.9} \qquad (37)$$

where Re_x is the Reynolds number based on the freestream velocity and a lengthscale x.

All grids used in this current work were generated with the distance from the wall to the first cell centre set to satisfy $y^+ \leq 1$ and approximately 20-30 gridpoints within $y^+ < 100$. For a Reynolds number around 2 million, based on freestream velocity and the airfoil chord length c, the former constraint gives a first cell height of the order $10^{-5}c$.

While constructing these grids care has also been taken to achieve wake distributions suitable for the actual flow conditions. This means that the cell-clustering downstream of the airfoil should, to the best possible extent, be aligned with the propagation of the physical viscous wake.

The farfield boundaries are placed approximately 10-15 c away from the airfoil in order to get a controlled overall stretching and a reasonable amount of points.

Drag Evaluation

For the aeronautical design of modern efficient wings and airfoils the aerodynamicists of today combine windtunnel measurements with the use of computational fluid dynamics (CFD).

During the last years several examples of the use of Navier-Stokes solvers in computing high-lift flows have been reported in the literature[13-15] with encouraging results. Future improvements in the detailed aerodynamic design, e.g. design of high-lift devices, will definitely include numerical optimization methods using Navier-Stokes solvers for the flow analysis.

In aerodynamic optimization problems the topic often is to minimize a cost function. This function can be, for example, the drag coefficient (C_d) or the ratio of drag to lift (C_d/C_l). It will become quite obvious that, to attain a meaningful and successful shape optimization, the analysis code must in the first place be able to accurately predict lift and drag.

Although much progress has been made in computing high-lift flows over multi-element airfoils using Navier-Stokes methods an accurate drag prediction seems to be quite problematic to achieve. Several articles reported lately in the literature[13-15] confirm this.

A general expression for the force F_i acting on an object with boundary surface B immersed in a fluid can be derived directly from the Navier-Stokes equations as

$$F_i = -\iint_S \rho U_i (U_j n_j)\, dS - \iint_S p n_i dS + \iint_S \tau_{ij} n_j dS \qquad (38)$$

where S is any surface enclosing the body. If this surface coincides with the airfoil contour the first integral vanishes and the forces are entirely given by surface integration of pressure and skin friction.

Integration of surface pressure and skin friction is what normally is done in most CFD codes when lift and drag are to be determined. This procedure works very well for calculating lift. However, drag is usually very small in comparison to lift, so even small uncertainties in surface pressure and skin friction may cause relatively large drag errors.

Another and theoretically more appealing approach for drag estimation would be to evaluate the total momentum deficit in the wake of the body. This is how it is often done in windtunnel measurements by a wake traversing procedure. Proceeding from equation (38) and by making some assumptions of the flow field, e.g. incompressible flow conditions, an expression for the drag coefficient entirely based on pressure terms may be derived[12]

$$C_d = 2\int \sqrt{\frac{P_t - p}{q_\infty}} \left(1 - \sqrt{\frac{P_t - p_\infty}{q_\infty}}\right) dy \qquad (39)$$

with the total pressure $P_t = p + q$ and the dynamic pressure defined as $q = 0.5\rho\,(U^2 + V^2)$.

This integral is evaluated over a limited section perpendicular to the freestream direction in the wake downstream of the airfoil.

Calculation of profile drag according to equation (39) is in the literature often referred to as the method of Jones[12] and it has been applied frequently in both wind tunnel and flight measurements with very satisfactory results.

In the following chapters dealing with computational results for multi-element airfoils special emphasis will be put on the drag prediction ability. Both the method of surface integration of pressure and skin friction and the method of Jones are used for comparison.

Validation Cases

Accurate predictions of airfoil flows at conditions near maximum lift are of prime industrial importance. Hence, the computational methods must be carefully validated against detailed measurements in order to quantify and improve their applicability and accuracy.

In the numerical solutions there are always errors which may come from physical modelling assumptions and/or numerical errors. Physical modelling errors include, among others, approximations introduced by a turbulence model. Into the category numerical errors falls effects from e.g. discretization schemes, added numerical dissipation and grid influences.

The code validation work aims to investigate and quantify influences on the solution originated from turbulence modelling, boundary conditions, artificial dissipation and grid resolution.

In Europe there have been different collaboration projects during the recent years with the objective of validating Navier-Stokes codes with respect to their ability to predict high-lift characteristics for single and multi-element airfoils.

The topic within BRITE/EURAM EUROVAL[13] was maximum lift investigations for single elements airfoils and study of high-lift flows for a two-element configuration.

For the study of the stall process the Aerospatiale airfoil A (fig. 2) was chosen with detailed experimental data available from the ONERA windtunnels F1 and F2.

High-lift flows were investigated around the NLR7301 flapped airfoil (fig. 3) with measurements done by Van den Berg[16-17] as comparisons. This wing/flap configuration has been derived from an early supercritical section, NLR7301, from which a flap has been 'cut out'.

The GARTEUR High-Lift Action Group AD (AG13)[18] is another research program where validation of CFD methods is an important issue. Here the A310 three-element airfoil (fig. 4) has been investigated in take-off configuration.

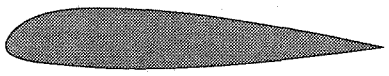

Fig. 2 Aerospatiale airfoil A

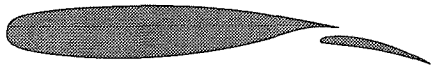

Fig. 3 NLR7301/Flap configuration

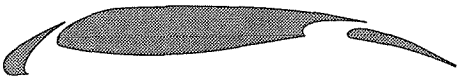

Fig. 4 A310 three-element airfoil

Computational Results

Single-Element Airfoil: Airfoil A

From the ONERA F2 windtunnel extensive boundary layer data is given for a lowspeed test case close to stall, where $M_\infty = 0.15$, $Re = 2.1 \cdot 10^6$ and $\alpha = 13.3°$.

This case is quite challenging since the measurements reveal a clear separated region near the trailing edge upper surface. Here, the turbulence is affected by streamline curvature and shows a strong non-isotropic character. Therefore, for this case, the turbulence modelling becomes crucial.

This flow case was computed applying both the two-layer κ-ε model (KE) and the Reynolds stress model (RSM) with transition points specified according to the observed locations in the experiments.

A structured single block C-mesh consisting of 384x64 cells with its wake cut extending from the trailing edge "flow-adapted" for this particular case was used in the computations (fig. 5).

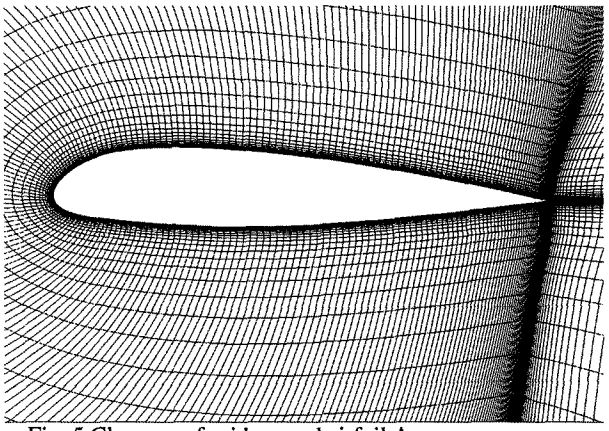

Fig. 5 Close-up of grid around airfoil A

The KE-results are very much in-line with previous results obtained by SAAB within the EUROVAL project[13] using the same turbulence model. The pressure distribution agrees well with the experiments except at the nose suction peak and in the trailing edge region (fig. 6). These discrepancies are mainly due to the inability of the κ-ε model to adequately capture the trailing edge separation. The skin friction plot (fig. 7) reveals that the κ-ε model hardly predicts any separated region at all.

The obtained RSM-results are somewhat better than the KE-results. The computed pressure distribution agrees well with the experiments even at the nose suction peak and in the trailing edge region (fig. 6). The discrepancy between the computed lift coefficient and the measured lift coefficient is small (an error around 1%). Considering the drag, a discrepancy around 5% is found.

The computed skin friction distribution (fig. 7) indicates that RSM estimates the streamwise extension of the trailing edge separation fairly well. However, the velocity profile (fig. 8) expose a much too thin backflow region near the trailing edge.

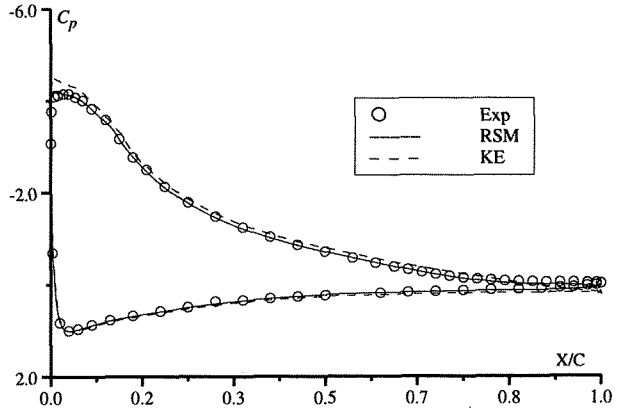

Fig. 6 C_p - distribution for airfoil A at $\alpha = 13.3°$

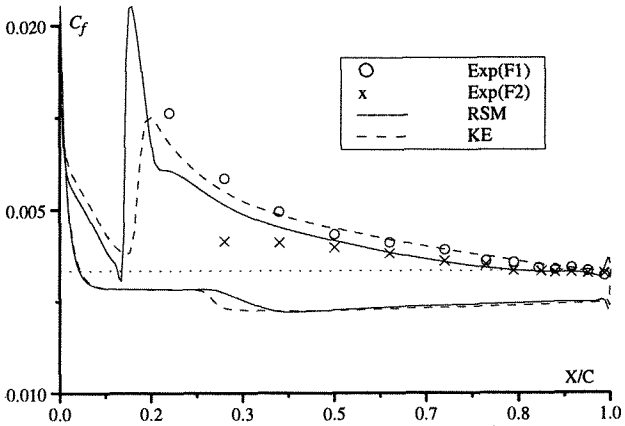

Fig. 7 C_f - distribution for airfoil A at $\alpha = 13.3°$

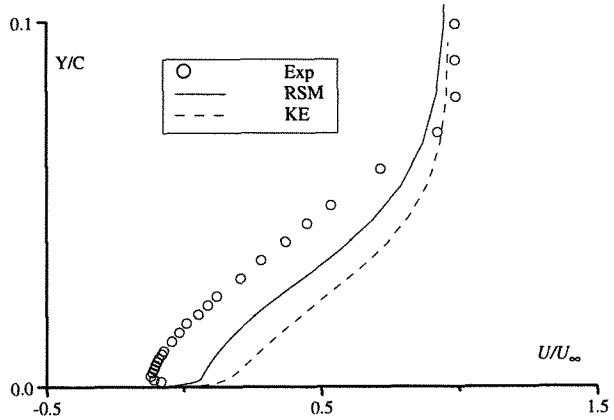

Fig. 8 Velocity profiles for airfoil A at x/c=0.96, at $\alpha = 13.3°$

In figure 9 the normal stresses near the trailing edge are plotted showing a pronounced anisotropy in both computed and measured normal stresses.

The computed displacement thickness δ^* agrees reasonably well with the measured one for both turbulence models applied (fig. 10).

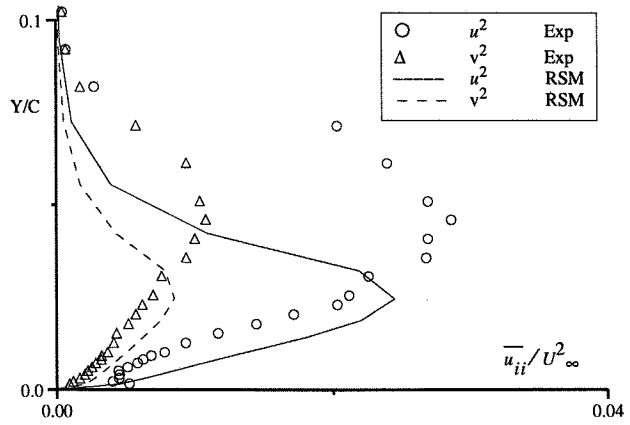

Fig. 9 Normal stresses for airfoil A at x/c=0.99, $\alpha = 13.3°$

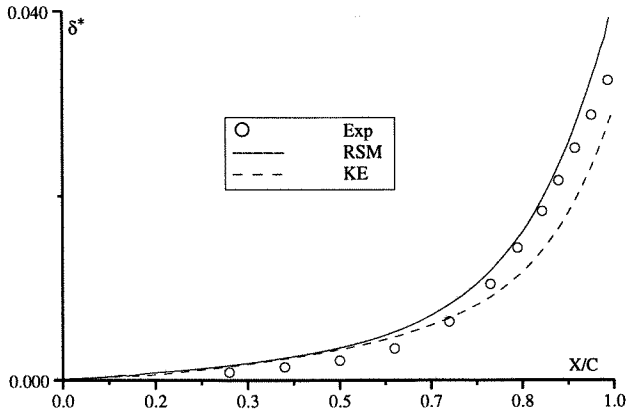

Fig. 10 Displacement thickness for airfoil A at $\alpha = 13.3°$

The lack of sensitivity to adverse pressure gradients and streamline curvature are well-known shortcomings of most κ-ε models and these results further confirm the apparent incapacity of these models to accurately treat airfoil flows involving trailing edge separation.

The RSM approach is physically more sound and some of the weaknesses of the eddy viscosity models may be overcome.

The current work indicates improvements in the computational results moving from a κ-ε model to a Reynolds stress model. However, the prediction of the trailing edge separation is still unsatisfactory.

The κ-ε model was run with the utilization of three levels of multigrid. A speed-up factor around 5 in CPU-time was observed using multigrid technique in comparison with a similar single grid calculation.

Two-Element Airfoil: NLR7301/Flap

Computations have been carried out with the free-stream conditions $M_\infty = 0.185$, $Re = 2.51 \cdot 10^6$. Two different angles of attack were studied, $\alpha = 13.1°$ with a gap width between main wing and flap of 2.6% c and $\alpha = 6.0°$ with a gap of 1.3% c. Here c denotes the retracted airfoil chord. The flap deflection angle was $\delta = 20°$ in both cases.

The grids used (fig. 11) consist of 11 blocks with a total number of 37 417 gridpoints.

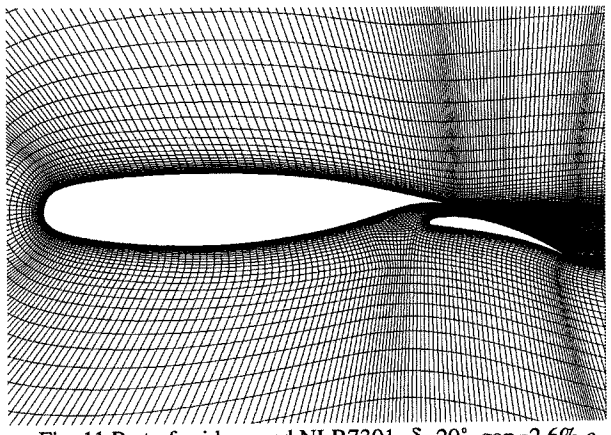

Fig. 11 Part of grid around NLR7301, δ=20°, gap=2.6% c

No flow separation occurs in these cases except for a small laminar separation bubble near the leading edge on the main wing. Hence, the turbulence modelling may not be as critical as for the single-element case. Nevertheless, for the smaller gap effects of confluent boundary layers are present and the $\alpha = 13.1°$ case is close to maximum lift making accurate predictions of these flow cases a rather demanding task.

The two-layer κ-ε model was applied with 20 cells within the inner layer and transition points specified according to the experimental observations.

Both cases computed reveal a laminar separation on the main wing upper surface roughly at the positions observed from the measurements (fig. 13a, b). The streamwise extension of the calculated separation bubble can be strongly influenced by the actual simulation of the laminar to turbulent transition process. In reality, the turbulent energy gradually increases in a transition region until the flow becomes fully turbulent.

In the current calculations transition is simply imposed at fixed positions. This may cause a rather abrupt increase in the eddy viscosity. Hence, to smooth this growth, the turbulent viscosity is made to vary linearly some short distance Δx in the streamwise direction.

Investigations indicate non-negligible effects of how the transition is applied in the laminar separation bubble. Small changes in the actual applied transition location and the ramp distance Δx used are found to significantly affect the computed extension of the bubble.

This separation will furthermore have an influence on the pressure distribution, note the double peak (fig. 12b).

In the measurements a thin laminar separation bubble being responsible for the transition to turbulent flow is found. Using a too long ramp distance Δx in the calculations may cause a rather large elongation of the obtained bubble.

In the current calculations transition to fully turbulent conditions is bound to occur over 1-2 grid cells.

The overall agreement between calculations and measurements is quite good for both cases (fig. 12-15).

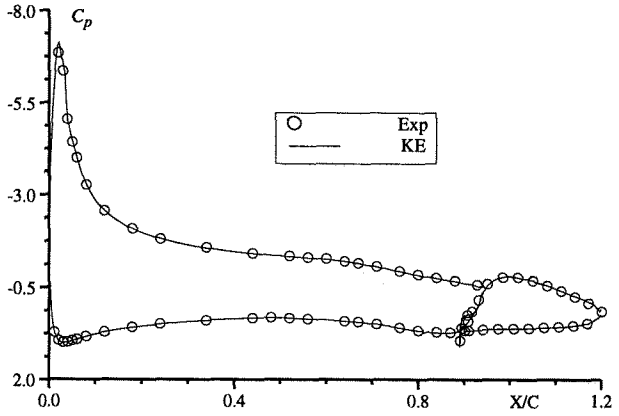

Fig. 12a C_p -distribution for NLR7301 at α=6.0°, gap=1.3% c

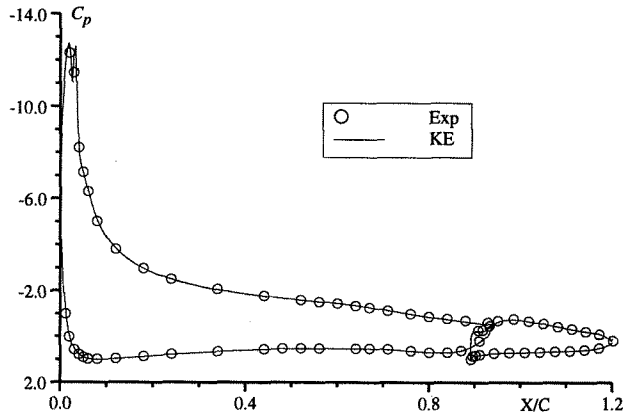

Fig. 12b C_p-distribution for NLR7301 at α=13.1°, gap=2.6% c

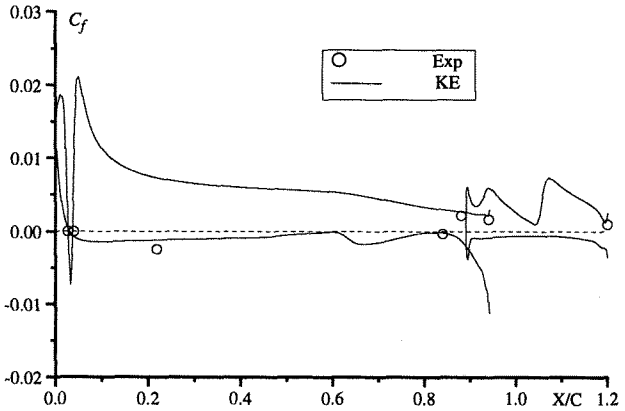

Fig. 13a C_f -distribution for NLR7301 at α=6.0°, gap=1.3% c

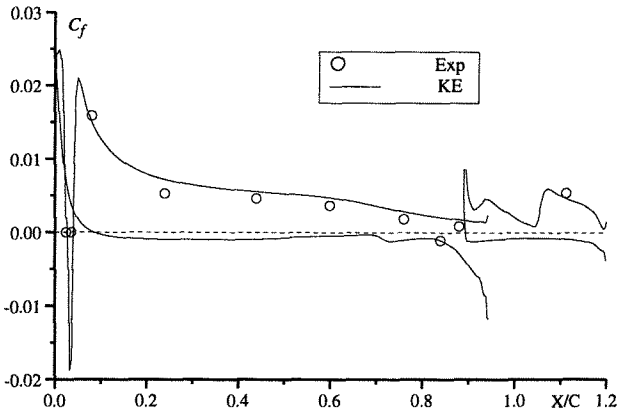

Fig. 13b C_f-distribution for NLR7301 at α=13.1°, gap=2.6% c

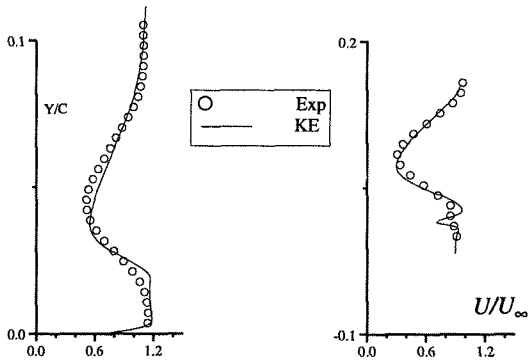

Fig. 14 Velocity profiles for NLR7301 at α=13.1°, gap=2.6% c, x/c=1.106 and x/c=1.295

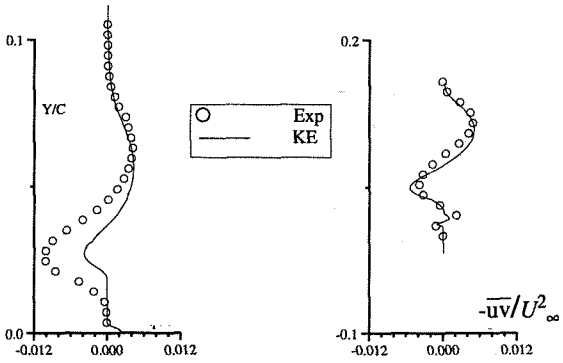

Fig. 15 Reynolds stress profiles for NLR7301 at α=13.1°, gap=2.6% c, x/c=1.106 and x/c=1.295

Drag Predictions. Within the EUROVAL project[13] all partners largely overpredicted (50%) the drag coefficient C_d although both surface pressure distributions and skin friction distributions in these computations agreed very well with the experimental ones.

Since the drag is order of magnitudes smaller than the lift even extremely small uncertainties in surface pressure and skin friction may cause relatively large drag errors while integrated over the airfoil surfaces. Therefore, drag errors

due to e.g. non-negligible influence from added numerical dissipation seem reasonable.

In the current calculations the artificial dissipation in the wall normal direction is scaled with the local Mach number. This will ensure reduced artificial dissipation in regions where the viscous dissipation is large, e.g. in the boundary layer near the airfoil surfaces. The computations ought to be driven very far to ensure that the final drag values are obtained from fully converged solutions.

Disturbances generated by a high-lift airfoil are transmitted long distances before damped out. Hence, the outer boundary should be placed at a sufficient distance, 50 chords or more, to ensure negligible disturbances to the uniform freestream. This is in many practical applications not possible since the amount of gridpoints needed will raise the computational time to an unacceptable level.

The total pressure losses, $P_{tloss} = 1 - P_t/P_{t\infty}$, plotted in figure 16 indicates that the use of freestream values, i.e. Γ=0, in the Riemann invariants applied at the farfield boundary is not satisfactory for high-lift calculations on the current grid, which has its outer boundary located around 10 chord lengths away from the airfoil.

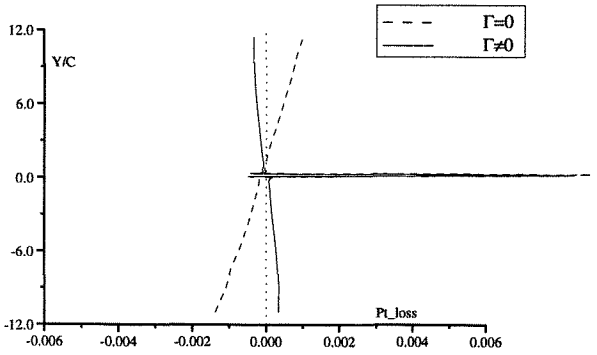

Fig. 16 Total pressure loss for NLR7301 at α=13.1°, gap=2.6% *c*, x/c=4.1

Using the circulation correction great improvements in drag predictions are found (table 1), whereas the lift coefficient hardly is affected at all. Earlier work concerning high-lift flows has also indicated similar improvements when using this circulation correction[19].

	α=6.0°	α=13.1°
$C_d(\Gamma=0)$	-	0.0626
$C_d(\Gamma\neq0)$	0.0282	0.0455
$C_{dwake}(\Gamma=0)$	-	?
$C_{dwake}(\Gamma\neq0)$	0.0220	0.0420
C_{dwake}**(exp)**	**0.0225**	**0.0445**

Table 1: Drag predictions for NLR7301

Another question arising from experiences made in the EUROVAL project[13] was whether the large discrepancies between computed drag and measured drag could be addressed to the different drag integration methods applied in the calculations and the measurements.

Since the experimental C_d value was obtained through a measuring of the momentum loss in the wake applying the method of Jones, a valuable investigation would be to try to simulate a similar procedure in the evaluation of C_d from the numerical solutions.

An algorithm has been implemented for drag evaluation according to the method of Jones. The centre of the wake is localized as the point of maximum total pressure loss and the integration interval is gradually expanded symmetrically ($\pm dy$) around the wake centre until a plateau in C_d is achieved. This integration was also performed at different streamwise locations.

Wake integration of the circulation corrected solutions show clear plateaus in C_d on levels very close to the experimental values (fig. 17a, b).

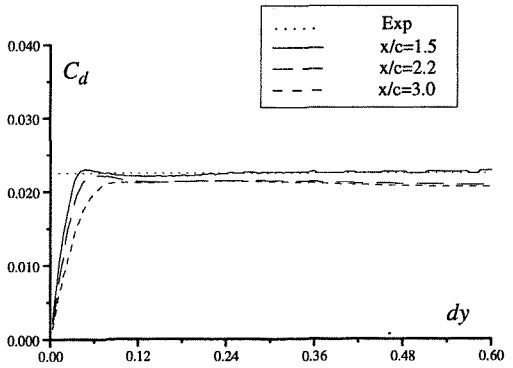

Fig. 17a Drag evaluation using the wake integration method of Jones, NLR7301, α=6.0° and Γ≠0

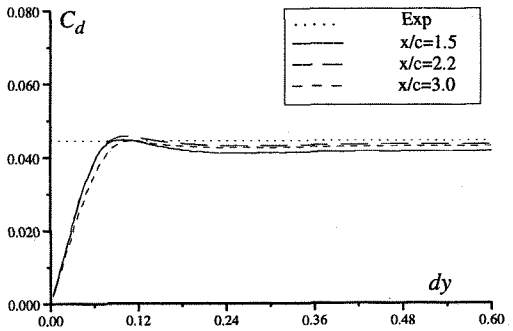

Fig. 17b Drag evaluation using the wake integration method of Jones, NLR7301, α=13.1° and Γ≠0

For the uncorrected case, however, the plateau is not as clear as for the corrected case. Also, a wider spreading is found in the results using different streamwise locations for the drag-integration of the uncorrected solution (fig. 18).

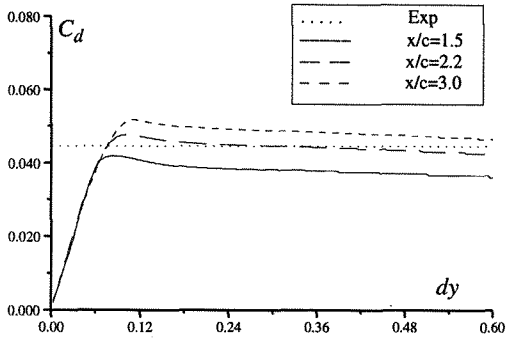

Fig. 18 Drag evaluation using the wake integration method of Jones, NLR7301, α=13.1° and Γ=0

Consequently, the circulation correction seems to be crucial for an accurate drag prediction regardless of integration method applied.

Three-Element Airfoil: A310

Within the GARTEUR high-lift research program[18] computations were made around the A310 three element airfoil in take-off configuration. This airfoil consisted of a leading edge slat deflected to $\delta_s = 20°$, a main element and a trailing edge flap with deflection $\delta_f = 16.7°$.

For this type of configuration large separation bubbles and significant confluence effects may occur. An accurate prediction of these effects is of prime importance since this can, to a large extent, affect the surface pressure distribution.

An advantage of using Navier-Stokes methods instead of the coupled viscid-inviscid approach is the potential of the former method to 'automatically' capture confluence and wake displacement effects without any further modelling of separation bubbles and wake flows which otherwise often is necessary.

A structured multiblock grid provided by DORNIER was used in the calculations. This grid is built up of 49 blocks with approximately 88 000 points in total (fig. 19).

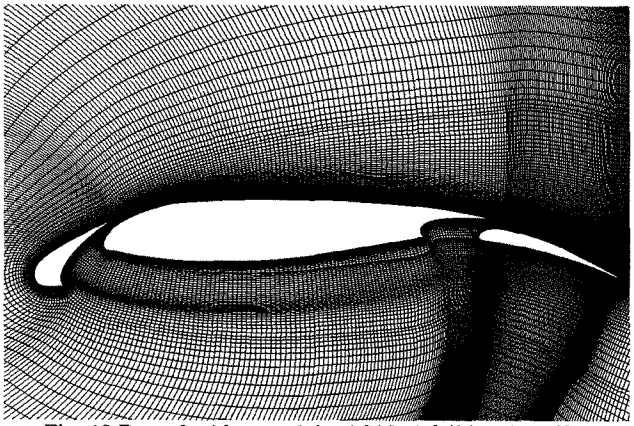

Fig. 19 Part of grid around the A310 airfoil in take-off configuration

The calculations were performed at freestream conditions $M_\infty = 0.22$, $Re = 1.9 \cdot 10^6$ and $\alpha = 12.2°$. The two-layer κ-ε model was applied and transition points specified according to the experimentally observed locations.

Fig. 20 Total pressure loss contours, A310, $\alpha = 12.2°$

Figure 20 shows total pressure loss contours where the appearance of the boundary layer mixing is seen. A large recirculation region containing several vortices can clearly be seen on the slat lower surface, fig. 21.

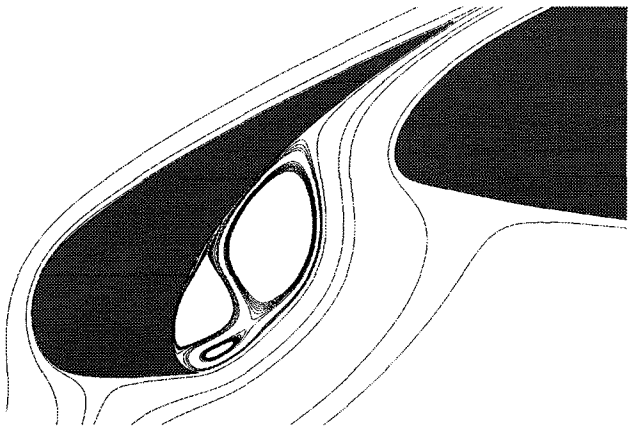

Fig. 21 Streamlines around the A310 slat-element, $\alpha = 12.2°$

The agreement between calculations and measurements is in general very good. Both skin-friction and surface pressure distributions computed compare well with experiments (fig. 22-23).

The laminar separation bubble observed on the slat upper surface is well predicted in the calculations as indicated in figure 23.

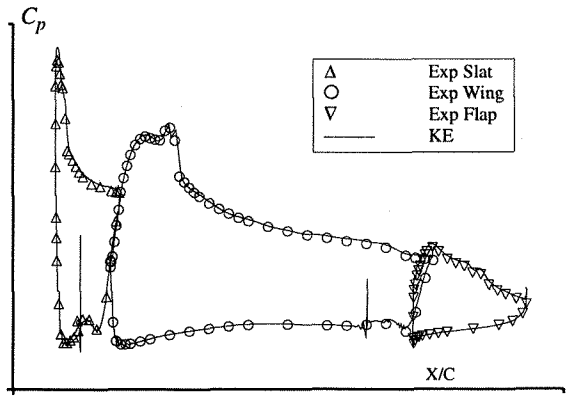

Fig. 22 C_p - distribution around A310, $\alpha = 12.2°$

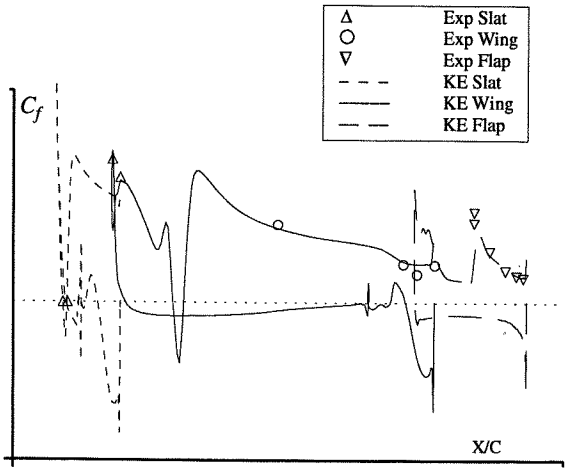

Fig. 23 C_f - distribution around A310, $\alpha = 12.2°$

Drag Predictions. Considering the integrated forces moment, lift and drag the discrepancies between measurements and calculations are less than 5%. Once again the circulation correction was shown to be a crucial factor for the drag results.

First the case was calculated without any circulation correction applied resulting in an overestimation of the drag with a factor more than two. By use of the circulation correction the computed drag falls very near the experimental value.

As was the case for the two-element airfoil, the experimental C_d value was obtained through a measuring of the momentum loss in the wake applying the method of Jones.

A wake integration of the circulation corrected solution shows a clear plateau in C_d on a level very close to the experimental value. For the uncorrected case, however, no plateau in C_d is achieved (fig. 24). The C_d value reaches a peak value on a level just above the experimental value and then drops down while expanding the integration interval further.

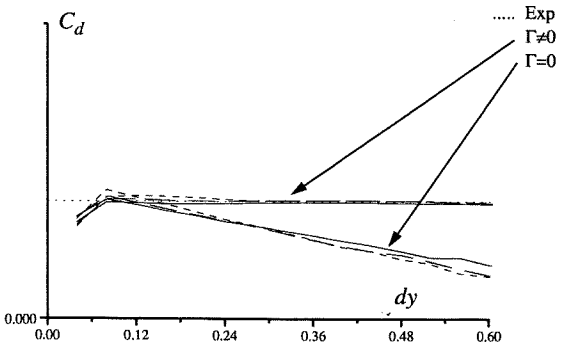

Fig. 24 Wake drag evaluation using the method of Jones, A310, $\alpha = 12.2°$

SAAB 2000 Applications

The design of the next generation of aircraft will need an increased use of accurate numerical methods. Reduction of the aerodynamic analysis time to acceptable levels requires fast numerical algorithms, high-speed computers, a highly developed geometry handler and grid generation system.

Within the SAAB 2000 project the 2d Navier-Stokes code NS2D has become a valuable and important engineering tool used as a complement to wind-tunnel experiments and flight tests.

An extensive numerical evaluation of the horizontal stabilizer including an aerodynamically balanced version of the elevator was accomplished in order to study effects from elevator and tab deflections as well as a variety of geometry modifications on both stabilizer and elevator.

Several grids had to be generated since each change in geometry or deflection angle necessitates a re-gridding. In the current work the ICEM CFD grid generator MULCAD [20] has been used. This grid generation system constitutes a flexible platform for controllable and accurate gridding.

These grids all included about 20 blocks with approximately 55 000 points in total. Figure 25 shows a close-up of the region around the elevator nose for a typical grid used in the Navier-Stokes calculations. Here the elevator has been deflected upwards with $\delta_e = -15°$.

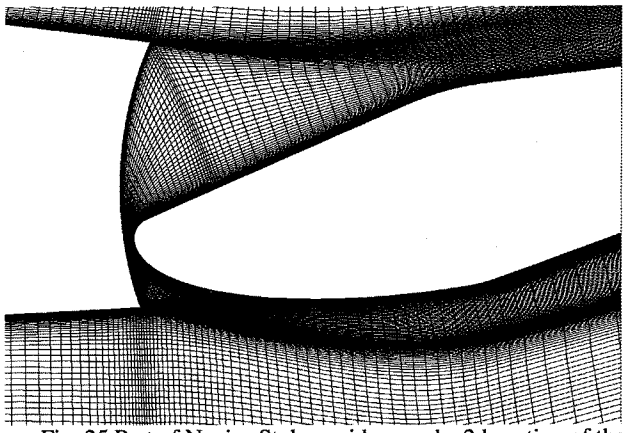

Fig. 25 Part of Navier-Stokes grid around a 2d-section of the SAAB 2000 stabilizer and aerodynamically balanced elevator

The main intention of this numerical survey of the stabilizer was to study its aerodynamic characteristics at cruise conditions. This means a freestream Mach number about $M_\infty = 0.60$ and a Reynolds number of $Re = 10 \cdot 10^6$. The angle of attack and the elevator deflection angle varied from -2° to +2°. However, also high-lift characteristics at low speeds were considered since the actual flight envelope to take into account is quite broad.

Figure 26 shows regions of separated flow for a low-speed case at a high angle of attack, $M_\infty = 0.20$, $Re = 5.5 \cdot 10^6$ and $\alpha = 14°$. The elevator deflection is $\delta_e = -15°$.

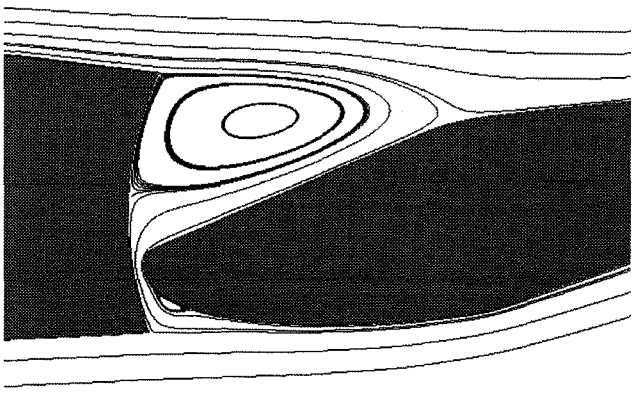

Fig. 26 Streamlines showing regions of separated flow between the SAAB 2000 stabilizer and elevator

Using the κ-ε model with three levels of multigrid a converged solution could be reached within two hours of CPU-time on a CRAY YMP. As convergence criteria both the rms-level of the conserved variables and the integrated lift coefficients for both stabilizer and elevator were used.

This investigation revealed the potential for improvement of the performance of the baseline configuration.

Based on displacement thickness distribution computed from the Navier-Stokes results a first reshaping of the stabilizer was made. This profile was further modified using an inverse facility included in the Navier-Stokes code[21].

This inverse design procedure is based on the modified Garabedian-McFadden algorithm[22] which is a residual correction technique. Here the residuals are the differences between the computed surface pressure distribution and the desired distribution.

The somewhat conflicting constraints of low high-speed drag and a given minimum lift at a large negative angle of attack in combination with geometrical constraints make such a shape design hard.

Significant improvements in aerodynamic performance were observed in the calculations for this modified profile. A clear drag reduction at cruise conditions (fig. 27) was seen in the computations which later on also was confirmed in both measurements and flight tests.

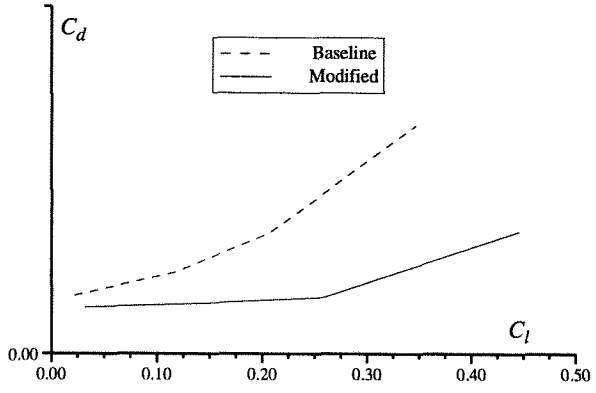

Fig. 27 C_d vs. C_l for the SAAB 2000 stabilizer

Not only the stabilizer but also the main wing profile including the flap have been thoroughly examined through Navier-Stokes analysis.

Here polars were calculated for a variety of configurations up to C_{lmax}. Different flap shapes as well as influence from varying the gap between wing and flap were examined.

Figure 28 illustrates a typical Navier-Stokes grid in the near flap region and figure 29 shows iso-Mach contours around the flap for a low-speed case.

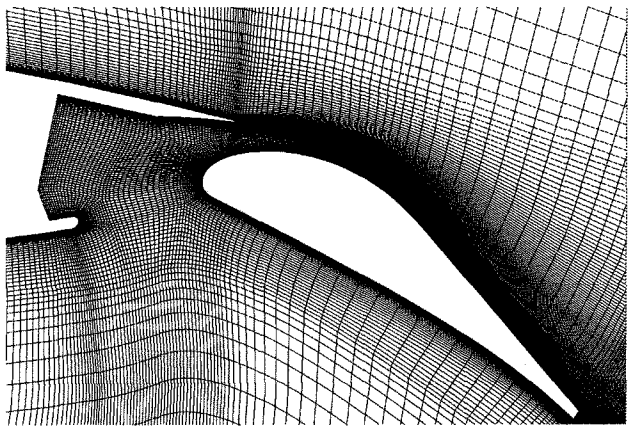

Fig. 28 Part of Navier-Stokes grid around a 2d-section of the SAAB 2000 wing including a trailing edge flap

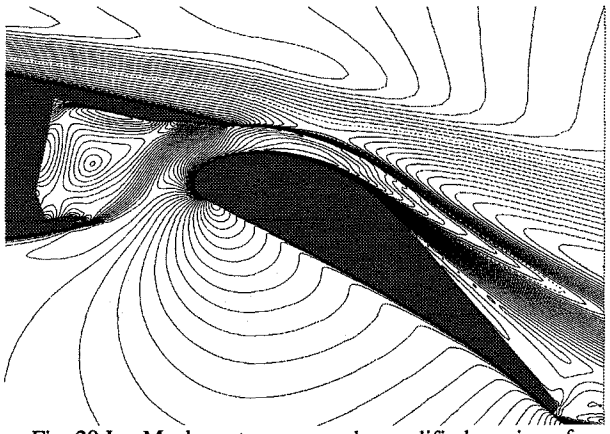

Fig. 29 Iso-Mach contours around a modified version of the SAAB 2000 flap

These numerical investigations of the SAAB 2000 wing and stabilizer constitute good examples of the beneficial in using Navier-Stokes methods for gaining deeper insight in complex flows which ultimately can lead to more optimized products.

Conclusions

The current work illustrates the large potential and applicability of Navier-Stokes methods for accurate predictions of high-lift flows around multi-element airfoils. With the utilization of multigrid technique a significant speed up can be achieved resulting in reasonable CPU-times making these methods applicable as engineering tools.

Very good agreement between calculations and measurements is found up to conditions near maximum lift.

Nevertheless, capturing of the stall process will inevitably demand further improvements in the field of turbulence modelling.

Special attention has been focused on drag calculation. By use of a circulation correction at the farfield boundary a great improvement is demonstrated in the drag prediction suggesting that the use of freestream values in the Riemann invariants is not satisfactory for high-lift calculations if not the outer boundary is placed very far away from the airfoil.

Both the method of surface integration of pressure and skin friction and the method of wake integration of momentum loss reveal a significant sensitivity on the farfield boundary conditions applied.

The obtained results indicate that the wake integration method can be successfully applied to high-lift flows over multi-element airfoils.

References

1 W. P. Jones and B. E. Launder, - The Prediction of Laminarisation with a Two-Equation Model of Turbulence, *Int. J. Heat Mass Transfer*, 15, 1972, pp. 301-314.

2 L. Davidson, -Implementation of a Semi-Implicit k-eps Turbulence Model into an Explicit Runge-Kutta Navier Stokes Code, Rept. TR/RF/90/26, CERFACS, 1990.

3 M. Wolfshtein, - The Velocity and Temperature Distribution in One-Dimensional Flow with Turbulence Augmentation and Pressure Gradient, *Int. J. Mass Heat Transfer*, 12, 1969, pp. 301-318.

4 L. Davidson, - Reynolds Stress Transport Modelling of Shock/Boundary-Layer Interaction, AIAA Paper No 93-2936, Orlando, 6-9 July, 1993.

5 J. C. Rotta, -Statistische Theorie nichthomogener Turbulenz, *Z. Phys.*, 129, 1951.

6 B. J. Daly and F. H. Harlow, - Transport equations of turbulence, *Phys. Fluids,* 13, pp. 2634-2649, 1970.

7 M. M. Gibson and B. A. Younis, - Calculation of Swirling Jets with a Reynolds Stress Closure, *Phys. Fluids*, 29, pp. 38-48, 1986.

8 C. M. Bergman and J. B. Vos, - A Multi Block Flow Solver for Viscous Compressible Flows, 9th GAMM conference on Numerical Methods in Fluid Mechanics, Lausanne, Switzerland, 25-27 September 1991.

9 S. V. Patankar, *Numerical Heat Transfer and Fluid Flow*, McGraw-Hill, 1980.

10 P. Å. Weinerfelt, - Multigrid Technique Applied to a Cell Vertex Scheme for Numerical Solution of the 2-D Euler Equations, Rept. TR/RF/90/44, CERFACS, 1990.

11 J. L. Thomas and M. D. Salas, -Far-Field Boundary Conditions for Transonic Lifting Solutions to the Euler Equations, *AIAA Journal*, Vol. 24, No.7, 1985.

12 H. Schlichting, -*Boundary Layer Theory*, McGraw-Hill, 4th edition, 1960.

13 EUROVAL, - A European Initiative on Validation of CFD Codes, W. Haase, F. Brandsma, E. Elsholz, M. Leschziner, D. Schwamborn (Eds.), *Notes on Numerical Fluid Mechanics*, Volume 42 (1993), Vieweg Verlag.

14 T. Larsson, - High-Lift Calculations Using Navier-Stokes Methods, *Computational Fluid Dynamics '92*, Volume 2, Ch. Hirsch et al. (Eds.), 1992, Elsevier Science Publishers B.V.

15 S. E. Rogers, - Progress In High-Lift Aerodynamic Calculations, AIAA Paper 93-0194, Jan. 1993.

16 B. van den Berg, - Boundary Layer Measurements on a Two-Dimensional Wing with Flap, NLR TR 79009 U, January, 1979.

17 J. H. M. Gooden and M. van Lent, - Hot-Wire Measurements in the Two-Dimensional Wing Wake Above a Trailing Edge Flap at a Condition Close to Maximum Lift, NLR CR 91038 C, January, 1991.

18 T. Larsson, - 2D Navier-Stokes Computations with the SAAB NS2D Code for the A310 Three Element Airfoil, WP-34, GARTEUR High-Lift Action Group AD(AG13), April, 1993

19 T. Larsson, - Drag Predictions for 2D High-Lift Airfoils, WP-35, GARTEUR High-Lift Action Group AD(AG13), September, 1993

20 ICEM CFD/CAE MULCAD, Version 3.1.1.1, Reference Manual, Control Data, 1993.

21 T. Larsson, - Airfoil Design by use of an Inverse Method incorporated into a Navier-Stokes Solver, SAAB PM, March, 1993.

22 J. B. Malone, J. C. Narramore and L. N. Sankar, - Airfoil Design Method Using the Navier-Stokes Equations, *Journal of Aircraft*, Vol 28, No. 3, pp. 216-224, 1990.